PHYSICS AND CHEMISTRY OF SOLID STATE
V. 27, No. 2 (2026) pp. 440-448
Section: Physics

DOI: 10.15330/pcss.27.2.440-448

Vasyl Stefanyk Carpathian National University

ФІЗИКА І ХІМІЯ ТВЕРДОГО ТІЛА
Т. 27, № 2 (2026) С. 440-448
Фізико-математичні науки

PACS: 78.67.Bf; 61.46.Df

ISSN 1729-4428 (Print)
ISSN 2309-8589 (Online)

Mazin Mohammed Mawat[1], Ahmed Namah Mohamed[2], Marwa Khalid Razaq[3], Jafer Fahdel Odah[1]

Structural, Optical, and Antimicrobial Characterization of Cr_2O_3 Nanoparticles Prepared by Pulsed Laser Ablation

[1]*Al-Karkh University of Science, College of Science, Baghdad, Iraq, mazin.alali@kus.edu.iq, hajasafa@kus.edu.iq*
[2]*Al-Muthanna University, College of science, Department of Physics, Al-Muthanna, Iraq, ahmednamah@mu.edu.iq*
[3]*University of Technology, Environmental Research Center, Baghdad, Iraq, marwa.k.razaq@uotechnology.edu.iq*

In this study, chromium oxide (Cr_2O_3) nanoparticles (NPs) synthesized by using pulsed laser ablation in liquid (PLAL), a simple, cost and effective method for producing high purity nanomaterials. Structural characterizations of Cr_2O_3 were using X-ray diffraction (XRD) and the results showed that obtaining pure eskolaite phase Cr_2O_3 with a rhombohedral crystal structure. Scanning electron microscopy (SEM) analysis, at low laser energies (300-400 mJ), revealed that this process tends to produce smaller and more dispersed particles, where the energy is sufficient for ablation but not so excessive as to cause large-scale particle fusion. In contrast, higher laser energies (500–600 mJ) result in larger particles with increased aggregation, likely due to higher thermal input, enhanced diffusion and renucleation of nanoparticles in the liquid medium. Optical studies have shown a slight increase in the energy gap with increasing laser power, due to the Burstein-Moss shift, where the Fermi level moves into the conduction band, altering the electronic transitions. Antibacterial activity analysis confirmed that is the nanoparticles have effective against Klebsiella pneumoniae, Escherichia coli, and Staphylococcus epidermidis. While there was a different interaction between chromium oxide nanoparticles and the cellular structure of microorganisms such as Candida albicans and Staphylococcus aureus, meaning that their activity decreased.

Keywords: Antimicrobial Activity, PLA, Chromium Oxide Nanoparticles, Optical Band Gap, Structure Characterization.

Received 22 March 2025; Accepted 14 June 2026; Published 30 June 2026.

Introduction

Chromium oxide nanoparticles (Cr_2O_3) have a wide range of applications because their exceptional physical and chemical properties, including a bandgap energy of approximately 3.4 eV, high melting temperature, and exceptional stability [1]. Cr_2O_3 nanoparticles are used in different fields, such as the production of green pigments [2], heterogeneous catalysts [3], thermal protection coatings [4], antibacterial agents [5], wear and resistant materials [6], photonics, and advanced colorants [7]. Cr_2O_3 sintering ability is limited, requiring specific sintering conditions to achieve optimal density, yet its have high melting point (2435ºC) [8]. Among chromium oxides, trivalent Cr_2O_3 NPs are considered the most stable [8].

Cr_2O_3 NPs can be prepared by using different methods, such as pulsed laser ablation in liquid (PLAL), a versatile and straightforward technique for producing a diverse range of nanomaterials with varying structures, compositions, morphologies, and forms, including ceramic and metal nanoparticles [9]. The first reported pulsed laser ablation technique was in 1987 by Patil et al. [10] for synthesizing iron oxide nanoparticles. Since then, PLAL has been widely utilized for the synthesis of numerous metallic nanoparticles and has found applications in industries such as food, biomedical, and electronics. By confining the manufactured nanoparticles directly within the liquid phase, PLAL technology is an environmentally friendly protocol that overcomes the limitations of traditional synthesis. The complete absence of hazardous reducing agents, faster reaction rates, and the

elimination of multi-stage processing are among the key advantages of this pathway, also this technology ensures high laboratory safety, minimal toxicity, and ease of product collection [11].

The addition of external effects has received considerable attention during pulsed laser ablation (PLAL) to increase nanoparticle production beyond conventional industrial capabilities. Mehdi and Khosravi [12] provided a clear example of this, successfully increasing the production of colloidal copper nanoparticles by applying an external electric field during ablation, where the improvement in both the surface plasmon resonance and the overall particle size distribution is directly related to the presence of this electric field, which was responsible for the increased concentration of nanostructures.

In addition, the variety of laser configurations provides distinct strategic advantages, greatly expanding the scope for manufacturing customized nanostructures, and recent studies indicate a significant breakthrough in nanomaterials fabricated using pulsed laser ablation in liquids (PLAL). For instance, the utility of pulsed laser ablation in liquids for engineering nanocatalysts was comprehensively evaluated by Forsythe et al [13]. Their work encompassed light-driven heterogeneous catalysis, thermochemical catalysis, and organic oxidation processes, along with energy-related transformations such as water oxidation, hydrogen production, oxygen or carbon dioxide reduction, and nitrogen reduction. In a similar vein, Fazio et al [14] delivered a targeted review centered on the deployment of laser-generated nanoparticles within specialized domains, including sensing, biomedicine, and catalysis. Meanwhile, the critical experimental parameters that govern the final dimensions of PLAL-synthesized gold nanoparticles were systematically investigated by Naser et al [15].

The assembly of nanostructures and the synthesis of nanocrystals via external field-assisted laser ablation in liquids were presented by Xiao et al. [16], and Zhang et al. [17] confirmed one of the benefits of fabricating colloidal metal nanostructures via laser ablation in the fields of clean energy, drilling, and sensing platforms. Jaleh et al. [18] synthesized advancements in environmental remediation through laser-mediated nanocomposite engineering. Consequently, PLAL has established itself as a premier synthesis route, largely because it avoids hazardous precursors to yield inherently stable, pure, and ligand free nanoparticles. This operational profile renders the technique both economically sustainable and eco-friendly when contrasted with classical chemical pathways [19]. In a typical experimental setup, a pulsed laser beam targets a chromium oxide pellet immersed within water or an alternative solvent [20]. This configuration drives the rapid quenching of dissociated atomic species right at the plasma liquid interface, a critical phenomenon that grants precise authority over the final physicochemical traits of the nanoparticles. For instance, Cr_2O_3 NPs have been synthesized using nanosecond pulsed lasers with varying power levels to ablate chromium oxide plates immersed in water. Studies have demonstrated that the size and shape of Cr_2O_3 NPs can be precisely controlled by adjusting laser pulse power and ablation wavelength [21].Finally, Al-Kattan et al. [22] analyzed the use of short-pulse lasers as a versatile tool for creating novel nano- and microstructures, as well as compositional analysis for addressing healthcare and well-being challenges. PLAL is considered environmentally friendly because it does not produce harmful chemical waste. In addition, it can be used with a wide range of materials without requiring significant changes in procedures compared to chemical methods that often require the use of toxic or hazardous chemicals, making them less environmentally sustainable. [11]

By extending this research, we also studied the effect of varying laser energies 300, 400, 500, and 600 [mJ] on Cr_2O_3 by the PLAL technique, and highly pure Cr_2O_3 nanoparticles were successfully produced by pulsed laser ablation in deionized water at room temperature. We also investigated the mechanism of the crystalline formation of Cr_2O_3 nanoparticles and the effects of varying laser energies on crystalline growth, optical characteristics, and antimicrobial activity. To our knowledge, this is the first report on the effect of the varying laser energies at 300, 400, 500, and 600 [mJ] on the Cr_2O_3 nanoparticles by the PLAL technique.

I. Experimental details

Figure 1 illustrates the experimental setup employed for the synthesis of Cr_2O_3 NPs via the pulsed laser ablation in liquid (PLAL) technique.

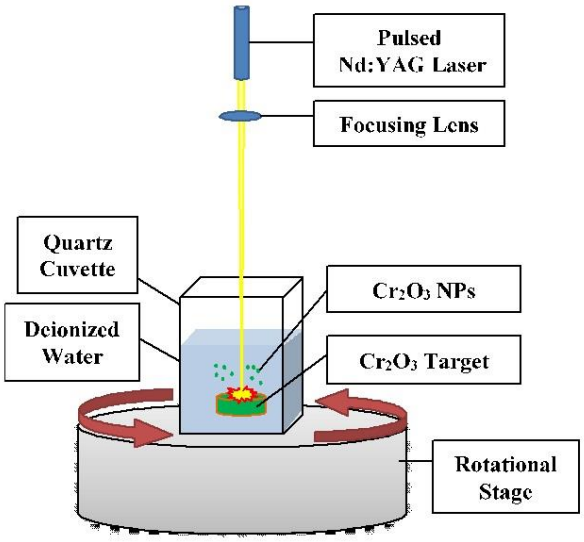

Fig. 1. Schematic diagram of the PLAL experimental setup utilized to synthesize Cr_2O_3 NPs.

The Cr_2O_3 NPs were grown via the pulsed laser ablation in liquid (PLAL) technique of commercially composed of high-purity chromium oxide powder (99.8% purity, American Elements Company), which was compressed into a pellet using a 20-ton hydraulic press, befor to ablation, the Cr_2O_3 target was meticulously cleaned with ethanol and rinsed with deionized water to eliminate surface contaminants. The process using nanosecond laser pulses from an A Q-switched Nd:YAG laser system, operating at a wavelength of 1064 nm with a pulse duration of 8 ns and a repetition rate of 1 Hz to generate colloidal Cr_2O_3 NPs dispersed in deionized

water, was utilized as the laser source, and the laser beam was collimated and focused onto the target using a plano-convex lens. Synthesis with laser pulse energies calibrated at 300, 400, 500, and 600 mJ. At each energy, a total of 500 laser pulses were delivered to secure an adequate yield of nanomaterial. To evaluate the structural and morphological properties of the Cr_2O_3 nanoparticles, X-ray diffraction XRD analysis was carried out using a Philips PW1050 diffractometer, and a SUPRA 55VP field emission scanning electron microscopy FESEM system. To investigate the optical characterizations of Cr_2O_3 nanoparticles, spectrophotometric measurements were executed using a Shimadzu 1200 double beam UV visible spectrophotometer. The antibacterial inclination of the Cr_2O_3 nanoparticles that were synthesized was estimated using agar well dispersion assay against four different bacterial strains (Staphylococcus aureus ATCC® 23235™, Klebsiella sp. ATCC® 13883™, Escherichia coli ATCC® 25922™, and Staphylococcus epidermidis ATCC® 12228™), and one type of fungi, Candida species (Candida albicans) – ATCC® 10231™) in accordance with the methodology outlined by [7]. All antibacterial tests were performed in triplicate (n = 3) under identical experimental conditions to ensure accuracy and reproducibility

PLAL is characterized by rapid preparation as nanoparticles can be produced within minutes or hours, depending on the experimental conditions compared to chemical methods which may require longer time due to the need for multi-step chemical reactions. [9]

II. Results and discussion

Figure 2. shows the XRD pattern of Cr_2O_3 NPs various laser energies.

The X-ray diffraction (XRD) pattern depicted in Figure 2 illustrates the as-synthesized Cr_2O_3 NPs through laser ablation at varying laser energies. The intensity peaks are positioned at 25.1, 33.4, 35.9, 39.6, 41.05, 50.07, 55.8, 63.2, and 65.1 diffraction angles, corresponding to reflections from (0 1 2), (1 0 4), (1 1 0), (0 0 6), (1 1 3), (0 2 4), (1 1 6), (2 1 4), and (3 0 0) reticular planes, respectively. These reflections are the fingerprints of the Cr_2O_3 crystalline lattice structure, which are attributed to rhombohedral structure (space group R-3c) with unit cell parameters a = 4.95876 Å and c = 13.59420 Å, Z = 6, of Eskolite pure Cr_2O_3 phase. These results agree with the Joint Committee on Powder Diffraction Standards (JCPDS) of the Cr_2O_3 structure card 00–038-1479 [23]. This alignment unequivocally affirms the crystallization of the eskolite-phase pure Cr_2O_3 structure, where the peaks are attributed to the rhombohedral configuration. The nanoparticles exhibited relatively strong crystalline peaks, and this is attributed to using varying laser pulse energies of 300-600 mJ, however, as the laser pulse energies increase from 300 to 600 mJ the diffraction peaks were significantly increased, especially the peaks at 25.1, 33.4, 35.9, 41.05, and 55.8◦. This could be due to the increase in laser pulse energies, and slight increase in the grain size [24].

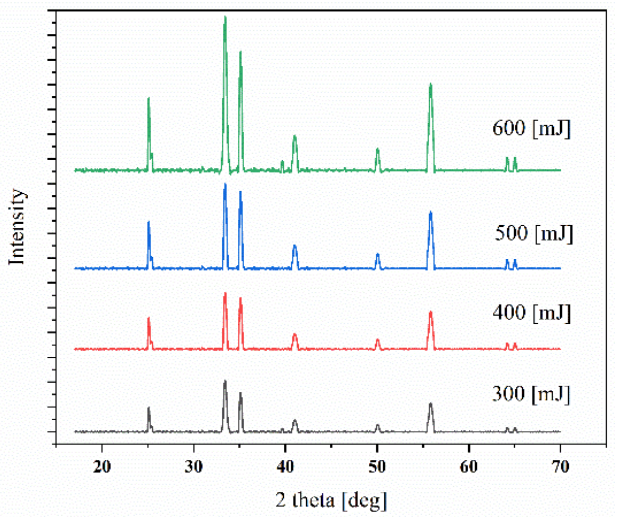

Fig. 2. XRD pattern of Cr_2O_3 NPs synthesized via pulsed laser ablation at 300, 400, 500 and 600 [mJ] laser energies.

The significant increase in the average crystal size (D) of the synthesized nanostructures, from 25.66 to 43.81 nm, provides evidence of a relationship between the use of higher laser energies during the synthesis process and the expansion in the crystal lattice parameters, as shown in the data in Table 1. This lattice expansion is consistent with structural expectations, driven primarily by the intrinsic ionic radius constraints of Cr3+ ions at 75.5 pm, which inherently dictates a lattice dilation, where this is consistent with the observations made in previous studies [25]. Additionally, the mechanism of resulting expansion in the crystal lattice parameters and charge density overlap between adjacent chromium and oxygen ions effectively reduces the formation of asymmetric bond lengths.

The average particle size of the Cr_2O_3 NPs was determined using Debye-Scherer's equation, which involves analyzing the diffraction line broadening of the main peaks [26]:

$$D = \frac{0.9\lambda}{\beta cos\theta} \quad (1)$$

Table 1.

Lattice parameters, crystallite size using gauss and W–H plot, strain, and dislocation density of C_2O_3 NPs synthesized via pulsed laser ablation at 300, 400, 500 and 600 [mJ] laser energies.

no. [mJ]	lattice parameter		Gauss crystallite size D [nm]	W-H plot crystallite size D_w [nm]	Strin, $\varepsilon\times10^{-3}$	Dislocation density, $\delta\times10^{-3}$
	a(Å)	c(Å)				
300	4.29317	13.6113	25.66	68	2.44	1.52
400	4.29385	13.782	26.77	57	2.16	1.39
500	4.29798	13.9818	30.82	54.8	1.62	1.05
600	4.3468	14.0663	43.81	49.11	1.2	0.52

where β is the full width at half maximum (FWHM) of intense peaks (in radians), λ is the X-ray wavelength source used (Cu-Kα = 0.15406 nm), and θ is the angle subtended in the peak.

The observed increase in the average crystallite size with the laser energies at which the samples were prepared suggests that this enhancement could be attributed to the incorporation of Cr^{3+} ions on the surface of Cr_2O_3 NPs.

The pulsed laser ablation method employed in the preparation of nanooxides induces structural disorder and lattice imperfections, including plane dislocations. The number of defects within the system can be determined by measuring the dislocation density (δ), which is defined as the length of the dislocation lines per unit volume in the crystal and can be found by formula (2) [27]:

$$\delta = \frac{1}{D} \tag{2}$$

where D is the crystallite size in nm.

The dislocation density decreases from 1.52×10^{-3} to 0.52×10^{-3}, As indicated in the table 1, which causes the formation of more defects and imperfections in the structure of lattice [28].

The Williamson-Hall (W-H) equation was used to determine the influence of microstrain (ε) present in synthesized powder samples, calculated via formula (3)

$$\beta cos\theta = \frac{0.9\lambda}{D} + 4\varepsilon\, sin\theta \tag{3}$$

The FWHM of the primary X-ray diffraction (XRD) peaks is denoted by β and is determined through Gaussian fitting of the experimental pattern. A graph is constructed with βcosθ on the y-axis and 4sinθ on the x-axis. The linear fitting of the graph intercept provides the crystallite size (D-W). The positive slope of the graph indicates the presence of tensile microstrain (ε) in Cr_2O_3 NPs. Table 1 shows the average crystallite size and microstrain as calculated by the Williamson-Hall (W-H) plot. A reduction in the microstrain value indicates the presence of structural flaws and disorders in the samples that were synthesized [29]. Notably, the crystallite size calculated using the W-H plot, accounting for microstrain impact, aligns with the trend observed using the Scherrer method. It is worth noting that the microstructural parameters, including microstrain (ε) and dislocation density (ρ), were extracted via Williamson–Hall (W–H) analysis based on a limited number of prominent diffraction peaks. Therefore, these calculated values are subject to some inherent limitations and experimental uncertainties. However, despite these significant limitations, the obtained data provide a highly accurate and reliable indication of the crystal behavior and structural evolution of the Cr_2O_3 lattice under the influence of different pulsed laser energies.

Figure 3 shown SEM images of the Cr_2O_3 nanoparticles at different laser energy of 300, 400, 500, and 600 mJ.

Figure 3a shows that the nanoparticles are predominantly spherical, with smaller nanoparticles

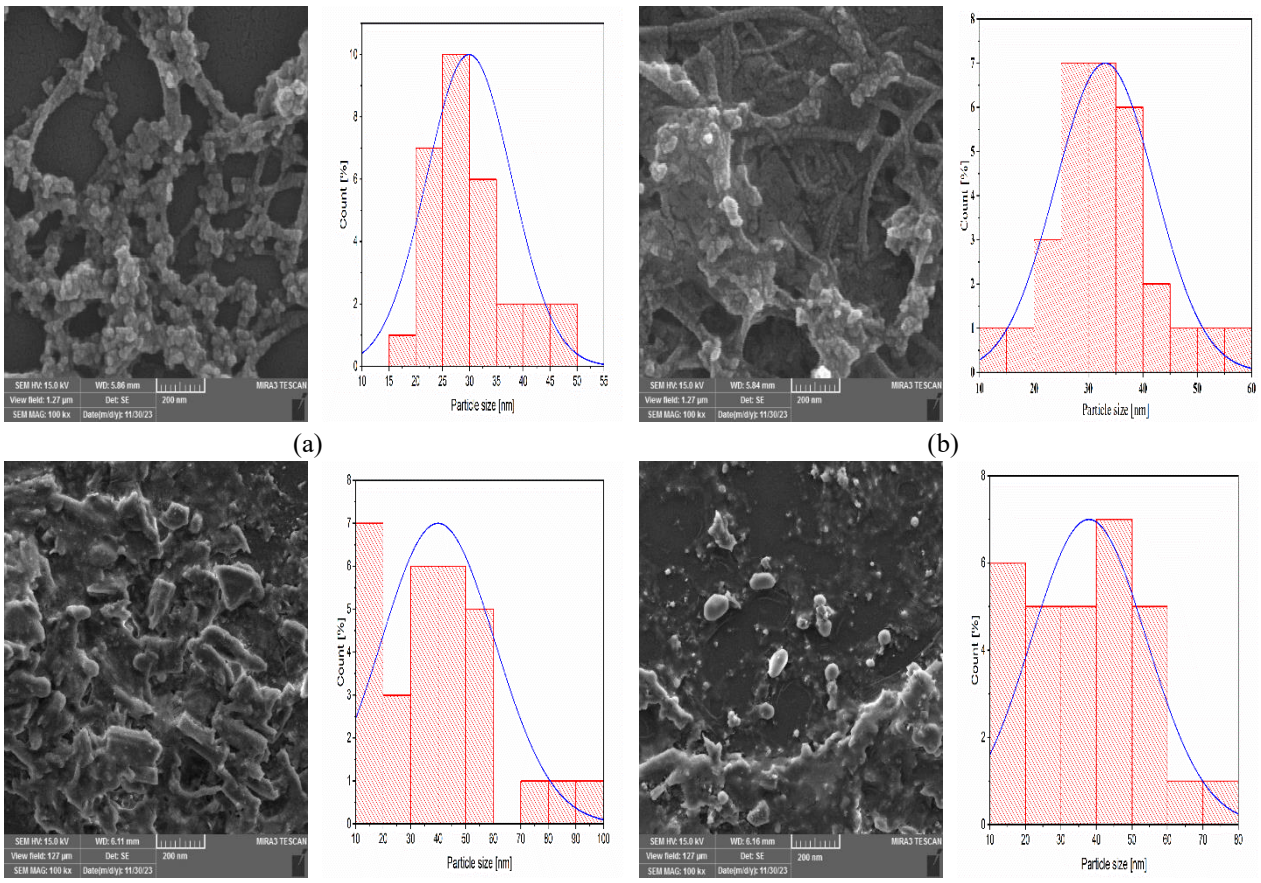

Fig. 3. SEM images of Cr_2O_3 NPs synthesized via pulsed laser ablation at (a)300 [mJ] (b) 400 [mJ] (c) 500 [mJ] (d) 600 [mJ] laser energies.

present. According to the corresponding graphs, a narrow size distribution is maintained, mainly between 20 and 50 nm. These preliminary data suggest that operating low laser energies reduces the density of the ablation material, inducing van der Waals forces to form larger aggregates [30]. Increasing the pulse energy to 400 mJ (Figure 3b) results in a clear morphological shift, with the Cr_2O_3 nanoparticles exhibiting a larger size distribution and a nanorod-like shape. Material extraction and plasma generation lead to structural elongation [31], causing the graph to shift to larger dimensions, between 30 and 60 nm. Crystallization and spatial reorganization within the liquid phase occur when high energy is introduced, accelerating the process. At the high energy threshold of 500 mJ (Figure 3c), the nanostructures adopt irregular shapes with rough and porous surfaces. In this case, the high energy density accelerates both the formation and evaporation rates, leading to particle fusion and subsequent pore formation [32]. The resulting size distribution is highly heterogeneous, with some nanostructures exceeding 60 nm in size, possibly due to the high energy density in the ablation region [33]. Ultimately, at the maximum energy of 600 mJ Figure 3d, a much larger and highly irregular morphology emerges, comprising a mixture of elongated and spherical entities. An increase in the average size of the nanoparticles was observed in the histogram, ranging from 30 to 65 nm. Consequently, it can be concluded that thermal effects become dominant at high laser energies, where the combination of high plasma temperatures and prolonged cooling periods promotes grain growth and particle agglomeration [34].

Various laser energies (300, 400, 500 and 600) mJ were used in the preparation of Cr_2O_3 NPs synthesized via pulsed laser ablation. The results revealed a variation in optical properties with different laser energies, as shown in Figure 4.

The optical band gap (Eg) was determined utilizing the Tauc relation, considering a direct transition between valence and conduction bands [35]. Figure 4 illustrates the Tauc plot, where the optical absorption coefficient (α) is correlated with the photon energy (hv) in semiconductors. The Tauc relationship is expressed as:

$$(\alpha h\upsilon)^{1/n} = A(h\upsilon - Eg) \qquad (4)$$

where A is constant, h is Planck's constant, and Eg is the band gap width.

n is a parameter that dependents on the nature of the transition. For direct allowed transitions n=1/2, while for indirect allowed transitions, n = 2 and for direct forbidden transitions n = 3/2.

The UV-Vis absorbance spectra of Cr_2O_3 nanoparticles (NPs) were recorded to examine their optical properties, as shown in Figure (4.a). The spectra exhibit distinct absorption peaks in the 230–250 nm and 350–380 nm regions, which are characteristic of electronic transitions in Cr_2O_3. The decrease in absorption at longer wavelengths is consistent with the wide band gap of the material. These peaks are attributed to the octahedral field symmetry, which induces the splitting of Cr^{3+} $3d^3$ orbitals into double degenerate and triple degenerate subbands.

Specifically, the absorbance peaks at 274, and 376 nm correspond to the $^4A_2g \rightarrow {}^4T_1g$ and $^4A_2g \rightarrow {}^4T_2g$ electronic transitions of Cr^{3+} ions, respectively. Additionally, these transitions are linked to the forbidden spin transitions of $^4A_2g \rightarrow {}^2T_1g$ and $^4A_2g \rightarrow {}^2Eg$. The presence of Cr^{6+} ions, which are associated with bulk Cr_2O_3 NPs, contributes to the observation of these bands.

The increased ablation rate resulting from higher laser power leads to a higher concentration of nanoparticles, which directly results in higher absorption of energy. The geometric dimensions of the nanostructures within the 30–50 nm range may play a role in determining the resulting spectral properties, and slight changes in the absorption peak may indicate the onset of a quantum confinement effect. Additionally, a slight Bursten-Moss shift can be observed, with a shift toward the conduction band and toward the Fermi level peak. This electronic arrangement widens the optical bandgap, thus pushing absorption toward shorter wavelengths.

These findings highlight the tunability of Cr_2O_3 NPs optical properties, which enhances their potential applications in optoelectronic devices and antimicrobial treatments [27].

The Cr2O3 nanoparticles exhibited a slight increase in their energy range under different laser power ranges, which is attributed to the Bursten-Moss effect [36]. In this study, the Fermi level was shifted to the forward direct conduction band, leading to optical absorption in the

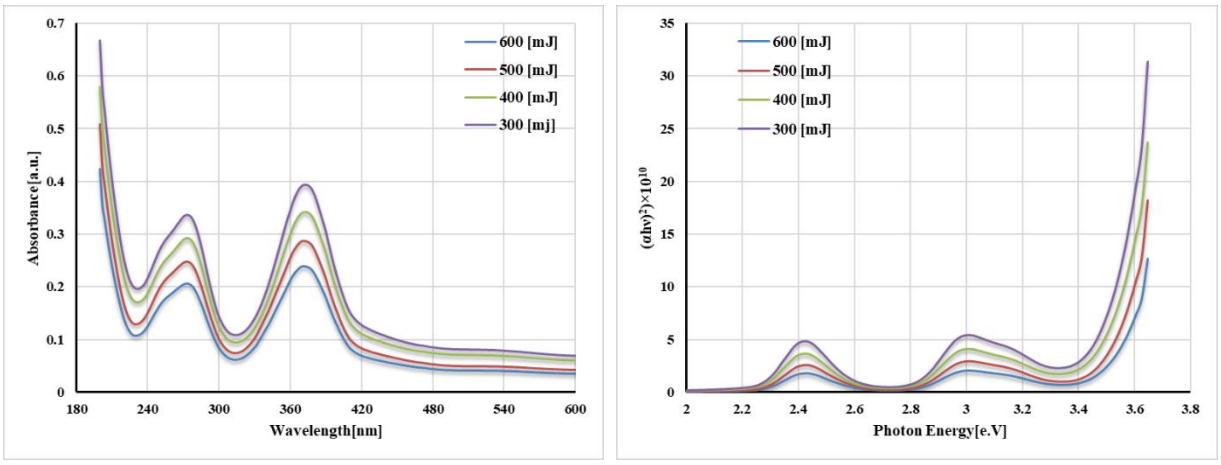

a) b)

Fig. 4. (a) Absorption spectra and (b) energy gaps of Cr_2O_3 NPs synthesized via pulsed laser ablation at 300, 400, 500 and 600 [mJ] laser energies.

vacuum band of the Fermi level from the valence band boundary. This phenomenon is due to the gradual accumulation of donor electrons filling the lower levels of the conduction band, thereby lowering the available electron transition thresholds. This contributes to an increased energy gap for Cr_2O_3 nanoparticles due to changes in the transition levels. Band gap for 300, 400, 500 and 600 mJ values respectively are 3.41, 3.44, 3.47, and 3.5 e.V.

Treatment of four types bacteria including (a) Klebsiella pneumonia, (b) Escherichia coli, (c) Staphylococcus epidermidis, (d) Staphylococcus aureus and one type fungi (e) Candida Species with Cr_2O_3 NPs synthesized via pulsed laser ablation at various laser energies, resulted in a decrease in bacterial growth, as shown in Figure 5 and listed in table (2).

The quantitative antimicrobial activity of the synthesized Cr_2O_3 nanoparticles was evaluated by measuring the inhibition zone diameters against various microbial strains, as summarized in Table. 2. The presented data includes the standard deviation (±SD) to illustrate the experimental precision and statistical variation of the zones of inhibition.

Chromium (III) oxide (Cr_2O_3) is a metal oxide with demonstrated antibacterial and antifungal properties, primarily attributed to its ability to release metal ions that interact with various components of microbial cells. These interactions damage the cell by disrupting key metabolic pathways, leading to structural damage to the cell membrane and cell death [37]. The antimicrobial activity of Cr_2O_3 nanoparticles has been shown to be highly sensitive to the membranes of both Gram-negative and Gram-positive cells, such as Staphylococcus epidermidis, Escherichia coli, and Klebsiella pneumoniae. In Gram-negative systems, the lipid-rich outer membrane normally acts as a protective barrier; however, it remains permeable to chromium ions or intact Cr_2O_3 compounds. Once inside the cell, these chemical compounds can compromise membrane integrity and disrupt essential cellular pathways, triggering a cascade of potent antibacterial reactions [38].

In contrast, the thick peptidoglycan structure characteristic of the cell membrane of Staphylococcus epidermidis bacteria paradoxically increases its susceptibility to the bactericidal effect of metal ions [39]. While exhibiting this behavior, Candida albicans fungi exhibit strong resistance against chromium trioxide nanoparticles. The reason for this resistance, which forms a strong physical barrier impeding the influx of Cr_2O_3 compounds, is the dense glycosidic structure of the fungal

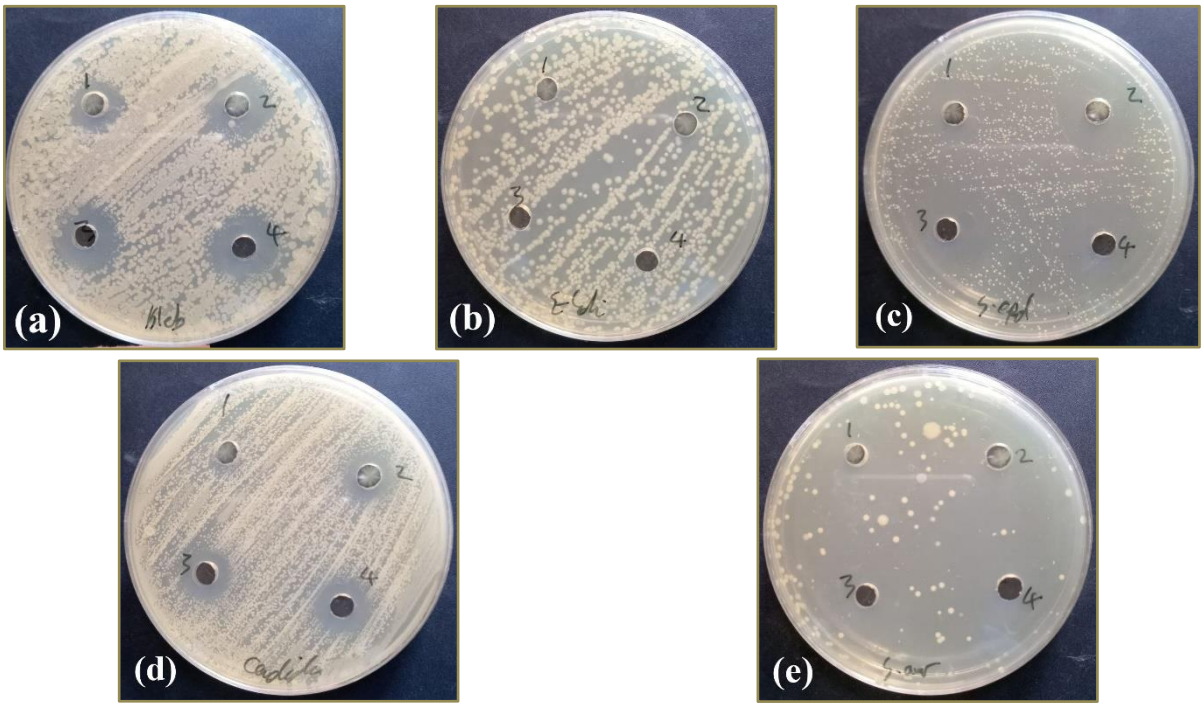

Fig. 5. Inhibition zones of Cr_2O_3 NPs against (a) Klebsiella sp., (b) Escherichia coli, (c) Staphylococcus epidermidis (d) Candida Species and (e) Staphylococcus aureus.

Table 2.
Inhibition zones of Cr_2O_3 NPs against Klebsiella sp., Escherichia coli, Staphylococcus epidermidis and Candida Species and Staphylococcus aureus

No.	Laser Energy (mJ)	Klebsiella pneumonia mm	Escherichia coli mm	Staphylococcus epidermidis mm	Candida albicans mm	Staphylococcus aureus mm
1	300	19.0 ± 0.5	23.0 ± 0.5	20.0 ± 1.0	12.0 ± 0.5	15.0 ± 0.5
2	400	17.0 ± 0.5	24.0 ± 1.0	20.0 ± 0.5	12.0 ± 0.5	16.0 ± 1.0
3	500	17.0 ± 1.0	23.0 ± 0.5	22.0 ± 0.5	13.0 ± 0.5	16.0 ± 0.5
4	600	17.0 ± 0.5	23.0 ± 1.0	22.0 ± 1.0	13.0 ± 0.5	17.0 ± 0.5

cell wall, thus reducing the effectiveness of the therapeutic compounds [40]. While Staphylococcus aureus secretes beta-lactamase enzymes to neutralize external stresses or form dense biofilms, this is a specialized survival strategy that resists the toxicity of metal oxides such as chromium trioxide and provides physical protection to cell populations. Therefore, overall, Candida albicans and Staphylococcus aureus utilize a defensive mechanism ranging from biofilm arrays to enhanced cell wall integrity to survive and remain unaffected by Cr_2O_3 toxicity, whereas the structural features of Klebsiella pneumoniae, Escherichia coli, and Staphylococcus epidermidis make their cell boundaries easily disrupted by gaseous metal ions [41].

Conclusion

The synthesis of chromium oxide nanoparticles via pulsed laser ablation in liquid (PLAL) was studied, a technique known for its ability to produce high purity nanomaterials. X-ray diffraction (XRD) analysis confirmed that the Cr_2O_3 crystalline phase was a pure scolite with a rhombic structure. The increased crystallinity and grain size resulted from varying the laser pulse energy from 300 to 600 mJ, leading to a larger grain size. Scanning electron microscopy (SEM) images revealed that lower energies (300–400 mJ) produced smaller, more uniformly distributed particles, while higher energies (500–600 mJ) produced larger, denser particles due to increased diffusion and recrystallization. According to the Ostwald maturation effect, laser energy determines the shape and aggregation; thus, the Cr_2O_3 transformed from a spherical to a rod-like nanostructure with moderate porosity. As a result of the high absorption and ablation rates, the concentration of nanoparticles increased with increasing laser power. The particle size range (30–50 nm) affected the spectral properties, and slight changes were observed in the Burstyn-Moss spectrum. Due to the high Fermi level, the absorption shifted towards shorter wavelengths (blue) and the band gap widened, indicating quantum confinement effects. Antibacterial activity analysis confirmed that is the Cr_2O_3 nanoparticles have strong effective against, Klebsiella pneumoniae, Escherichia coli, and Staphylococcus epidermidis due to its ability to disrupt bacterial cell membranes and intracellular processes. Conversely, with regard to Candida albicans and Staphylococcus aureus, the antimicrobial activity decreased due to enhanced cell wall integrity and biofilm formation.

Conflict of Interest Statement:

The authors declare that there is no conflict of interest regarding the publication of this manuscript. This statement indicates that the authors have no financial, personal, or professional conflicts that could have influenced the research or its outcomes.

Mawat Mazin Mohammed – Assistant professor, Dr.;
Mohamed Ahmed Namah – Assistant professor, Dr.;
Razaq Marwa Khalid – Lecturer, Dr.;
Odah Jafer Fahdel – Professor, Dr.

[1] J. Iqbal, B. A. Abbasi, A. Munir, S. Uddin, S. Kanwal, & T. Mahmood, Facile green synthesis approach for the production of chromium oxide nanoparticles and their different in vitro biological activities. Microscopy research and technique, 83(6), 706 (2020); https://doi.org/10.1002/jemt.23460.

[2] S. Ghotekar, S. Pansambal, M. Bilal, S.S. Pingale, & R. Oza, *Environmentally friendly synthesis of Cr_2O_3 nanoparticles: characterization, applications and future perspective─ a review*. Case Studies in Chemical and Environmental Engineering, 3, 100089 (2021); https://doi.org/10.1016/j.cscee.2021.100089.

[3] B. M. Abu-Zied, *Structural and catalytic activity studies of silver/chromia catalysts*. Applied Catalysis A: General, 198(1-2), 139 (2000). https://doi.org/10.1016/S0926-860X(99)00508-6.

[4] O. Muller, M. Guerchoux, P. Gibot, L. Merlat, & D. Spitzer, *Optical limiting and nonlinear optical properties of Cr_2O_3 and WO 3 based polymer nanocomposites.* Optics Continuum, 1(11), 2389 (2022); https://doi.org/10.1364/OPTCON.474445.

[5] P. Gibot, & L. Vidal, *Original synthesis of chromium (III) oxide nanoparticles*. Journal of the European Ceramic Society, 30(4), 911 (2010); https://doi.org/10.1016/j.jeurceramsoc.2009.09.019.

[6] H. Kitsunai, K. Hokkirigawa, N. Tsumaki, & K. Kato, *Transitions of microscopic wear mechanism for Cr_2O_3 ceramic coatings during repeated sliding observed in a scanning electron microscope tribosystem*. Wear, 151(2), 279 (1991); https://doi.org/10.1016/0043-1648(91)90255-S.

[7] S.A. Khan, S. Shahid, S. Hanif, H.S. Almoallim, S.A. Alharbi, & H. Sellami, *Green synthesis of chromium oxide nanoparticles for antibacterial, antioxidant anticancer, and biocompatibility activities*. International Journal of Molecular Sciences, 22(2), 502. (2021); https://doi.org/10.3390/ijms22020502.

[8] S. A. Rakesh, & N.M.M. Gowda, *Synthesis of Chromium (III) Oxide Nanoparticles by Electrochemical Method and Mukia Maderaspatana Plant Extract, Characterization, $KMnO_4$ Decomposition and Antibacterial Study*. Imperial Journal of Interdisciplinary Research, (37), (2016); https://doi.org/10.4236/mrc.2013.24018.

[9] H. Zeng, X.W. Du, S.C. Singh, S.A. Kulinich, S. Yang, J.He, & W. Cai, *Nanomaterials via laser ablation/irradiation in liquid: a review*. Advanced Functional Materials, 22(7), 1333 (2012); https://doi.org/10.1002/adfm.201102295.

[10] PP Patil, DM Phase, SA Kulkarni, SV Ghaisas, SK Kulkarni, SM Kanetkar, SB Ogale, VG Bhide. *Pulsed-laser-induced reactive quenching at liquid-solid interface: Aqueous oxidation of iron*. Phys Rev Lett. 1987 Jan 19; 58(3), 238(1987); https://doi.org/10.1103/PhysRevLett.58.238.

[11] G.W. Yang, *Laser ablation in liquids: Applications in the synthesis of nanocrystals*. Progress in Materials Science, 52(4), 648(2007); https://doi.org/10.1016/j.pmatsci.2006.10.016.

[12] M.H. Mahdieh, & A. Khosravi, *Colloidal brass nanoparticles produced by pulsed laser ablation in deionized water and the effect of external electric field on particle size characteristics and ablation rate*. Nano-Structures & Nano-Objects, 24, 100580 (2020); https://doi.org/10.1016/j.nanoso.2020.100580.

[13] R. C. Forsythe, C.P. Cox, M. K.Wilsey, & A.M. Muller, *Pulsed laser in liquids made nanomaterials for catalysis*. Chemical Reviews, 121(13), 7568 (2021); https://doi.org/10.1021/acs.chemrev.0c01069.

[14] E. Fazio, B. Gökce, A. De Giacomo, M. Meneghetti, G. Compagnini, M. Tommasini, ... & F. Neri, *Nanoparticles engineering by pulsed laser ablation in liquids: Concepts and applications*. Nanomaterials, 10(11), 2317(2020); https://doi.org/10.3390/nano10112317.

[15] H. Naser, H. M. Shanshool, & K.I. Imhan, *Parameters affecting the size of gold nanoparticles prepared by pulsed laser ablation in liquid*. Brazilian Journal of Physics, 51(3), 878 (2021); https://doi.org/10.1007/s13538-021-00875-x.

[16] J.Xiao, P. Liu, C. X. Wang, & G.W. Yang, *External field-assisted laser ablation in liquid: An efficient strategy for nanocrystal synthesis and nanostructure assembly*. Progress in Materials Science, 87, 140 (2017); https://doi.org/10.1016/j.pmatsci.2017.02.004.

[17] J. Zhang, J. Claverie, M. Chaker, & D. Ma, *Colloidal metal nanoparticles prepared by laser ablation and their applications.* ChemPhysChem, 18(9), 986 (2017); https://doi.org/10.1002/cphc.201601220.

[18] B. Jaleh, M. Nasrollahzadeh, B.F. Mohazzab, M. Eslamipanah, M. Sajjadi, & H. Ghafuri, *State-of-the-art technology: Recent investigations on laser-mediated synthesis of nanocomposites for environmental remediation*. Ceramics International, 47(8), 10389(2021); https://doi.org/10.1016/j.ceramint.2020.12.197.

[19] A. Subhan, A.H.I.Mourad, & Y. Al-Douri, *Influence of laser process parameters, liquid medium, and external field on the synthesis of colloidal metal nanoparticles using pulsed laser ablation in liquid: A review.* Nanomaterials, 12(13), 2144 (2022); https://doi.org/10.3390/nano12132144.

[20] M. Honda, T. Goto, T. Owashi, A. G. Rozhin, S. Yamaguchi, T. Ito, & S.A. Kulinich, *ZnO nanorods prepared via ablation of Zn with millisecond laser in liquid media*. Physical Chemistry Chemical Physics, 18(34), 23628 (2016); https://doi.org/10.1039/c6cp04556a.

[21] T.M. Rashid, U.M. Nayef, M.S. Jabir, & F.A.H. Mutlak, *Synthesis and characterization of Au: ZnO (core: shell) nanoparticles via laser ablation*. Optik, 244, 167569 (2021); https://doi.org/10.1016/j.ijleo.2021.167569.

[22] A. Al-Kattan, D. Grojo, C. Drouet, A. Mouskeftaras, P. Delaporte, A. Casanova, ... & J. Hermann, *Short-pulse lasers: A versatile tool in creating novel nano-/micro-structures and compositional analysis for healthcare and wellbeing challenges*. Nanomaterials, 11(3), 712 (2021); https://doi.org/10.3390/nano11030712.

[23] A.B. Khelifa, A. Soum-Glaude, S. Khamlich, H. Glénat, M. Balghouthi, A. A. Guizani,... & W. Dimassi, *Optical simulation, characterization and thermal stability of Cr_2O_3/Cr/Cr_2O_3 multilayer solar selective absorber coatings.* Journal of Alloys and Compounds, 783, 533 (2019); https://doi.org/10.1016/j.jallcom.2018.12.286.

[24] M.G. Tsegay, H.G. Gebretinsae, G.G. Welegergs, M. Maaza, & Z.Y. Nuru, *Novel green synthesized Cr_2O_3 for selective solar absorber: Investigation of structural, morphological, chemical, and optical properties*. Solar Energy, 236, 308 (2022); https://doi.org/10.1016/j.solener.2022.03.011.

[25] J. Singh, V. Verma, & R. Kumar, *Preparation and structural, optical studies of Al substituted chromium oxide (Cr_2O_3) nanoparticles*. Vacuum, 159, 282 (2019); https://doi.org/10.1016/j.jmrt.2021.01.007.

[26] V.D. Mote, Y. Purushotham, & B.N. Dole, *Williamson-Hall analysis in estimation of lattice strain in nanometer-sized ZnO particles.* Journal of theoretical and applied physics, 6, 1 (2012); https://doi.org/10.1186/2251-7235-6-6.

[27] P. Bhardwaj, J. Singh, R. Kumar, R. Kumar, & V. Verma, *Structural, optical and magnetic characterization of Ni2+ ions doped chromium oxide (Cr2O3) nanoparticles*. Solid State Sciences, 115, 106581 (2021); https://doi.org/10.1016/j.solidstatesciences.2021.106581.

[28] A.K. Rana, Y. Kumar, P. Rajput, S.N. Jha, D. Bhattacharyya, & P.M. Shirage, *Search for origin of room temperature ferromagnetism properties in Ni-doped ZnO nanostructure.* ACS Applied Materials & Interfaces, 9(8), 7691 (2017); https://doi.org/10.1021/acsami.6b12616.

[29] S. Muthukumaran, & R. Gopalakrishnan, *Structural, FTIR and photoluminescence studies of Cu doped ZnO nanopowders by co-precipitation method*. Optical Materials, 34(11), 1946 (2012); https://doi.org/10.1016/j.optmat.2012.06.004.

[30] A.A. Myint, H.W. Lee, B. Seo, W.S. Son, J. Yoon, T.J. Yoon, ... & Y.W. Lee, *One pot synthesis of environmentally friendly lignin nanoparticles with compressed liquid carbon dioxide as an antisolvent*. Green Chemistry, 18(7), 2129 (2016); https://doi.org/10.1039/C5GC02398J.

[31] H. Wang, W. Han, X. Li, B. Liu, H. Tang, & Y. Li, *Solution combustion synthesis of Cr2O3 nanoparticles and the catalytic performance for dehydrofluorination of 1, 1, 1, 3, 3-pentafluoropropane to 1, 3, 3, 3-tetrafluoropropene*. Molecules, 24(2), 361(2019); https://doi.org/10.3390/molecules24020361.

[32] A.O. El-Gendy, Y. Obaid, E. Ahmed, C.S. Enwemeka, M. Hassan, & T. Mohamed, *The antimicrobial effect of gold quantum dots and femtosecond laser irradiation on the growth kinetics of common infectious eye pathogens: an in vitro study.* Nanomaterials, 12(21), 3757. (2022); https://doi.org/10.3390/nano12213757.

[33] K. Wantana, P. Aniwat, S. Bunlue, T. Alongkot, K. Anusit, & K. Pisist, *Study of thin film coating technique parameters for low cost organic solar cells fabrication.* Materials Today: Proceedings, 4(5), 6626 (2017); https://doi.org/10.1016/j.matpr.2017.06.177.

[34] E. Sadri, & F. Ashrafizadeh, *Structural characterization and mechanical properties of plasma sprayed nanostructured Cr_2O_3-Ag composite coatings.* Surface and Coatings Technology, 236, 91 (2013); https://doi.org/10.1016/j.surfcoat.2013.09.033.

[35] C.S. Vall, M. Chaik, A. Tchenka, S. Hnawi, A. Mellalou, M. Aggour, & A. Outzourhit, *Effect of chromium percentage doping on the optical, structural, morphological and electrical properties of ZnS: Cr thin films*, Physica E: Low-dimensional Systems and Nanostructures, 130, 114694 (2021); https://doi.org/10.1016/j.physe.2021.114694.

[36] J. Kaur, M. Sharma, O.P. Pandey, *Photoluminescence and photocatalytic studies of metal ions (Mn and Ni) doped ZnS nanoparticles*. Optical Materials, 47, 7 (2015); https://doi.org/10.1016/j.optmat.2015.06.022.

[37] S.M. Dizaj, F. Lotfipour, M. Barzegar-Jalali, M. H. Zarrintan, & K. Adibkia, *Antimicrobial activity of the metals and metal oxide nanoparticles*. Materials Science and Engineering: C, 44, 278 (2014); https://doi.org/10.1016/j.msec.2014.08.031.

[38] P.O.O.N.A.M. Sangwan, & H. Kumar, *Synthesis, characterization, and antibacterial activities of chromium oxide nanoparticles against Klebsiella pneumoniae*. Synthesis, 10(2) (2017); https://doi.org/10.22159/ajpcr.2017.v10i2.15189.

[39] A. Azam, A.S. Ahmed, M. Oves, M.S. Khan, S.S. Habib, & A. Memic, *Antimicrobial activity of metal oxide nanoparticles against Gram-positive and Gram-negative bacteria: a comparative study*. International journal of nanomedicine, 6003 (2012); https://doi.org/10.2147/IJN.S35347.

[40] L.E. Garcia-Marin, K. Juarez-Moreno, A.R. Vilchis-Nestor, & E. Castro-Longoria, *Highly antifungal activity of biosynthesized copper oxide nanoparticles against Candida albicans*. Nanomaterials, 12(21), 3856 (2022); https://doi.org/10.3390/nano12213856.

[41] H. Algadi, M.A. Alhoot, A.R. Al-Maleki, & N. Purwitasari, *Effects of Metal and Metal Oxide Nanoparticles against Biofilm-Forming Bacteria: A systematic Review.* Journal of Microbiology and Biotechnology, 34(9), 1748. (2024); https://doi.org/10.4014/jmb.2403.03029.

Мазін Мохаммед Мават[1], Ахмед Намах Мохамед[2], Марва Халід Разак[3], Джафер Фахдель Ода

Структурні, оптичні та антимікробні властивості наночастинок Cr_2O_3, отриманих методом імпульсної лазерної абляції

[1]*Університет науки Аль-Кархх, Коледж наук, Багдад, Ірак, mazin.alali@kus.edu.iq, hajasafa@kus.edu.iq*
[2]*Університет Аль-Мутанна, Коледж наук, кафедра фізики, Аль-Мутанна, Ірак, ahmednamah@mu.edu.iq*
[3]*Технологічний університет, Центр екологічних досліджень, Багдад, Ірак, marwa.k.razaq@uotechnology.edu.iq*

У даному дослідженні наночастинки оксиду хрому (Cr_2O_3) синтезовано методом імпульсної лазерної абляції в рідині (PLAL), який є простим, економічно ефективним методом отримання наноматеріалів високої чистоти. Структурні характеристики Cr_2O_3 досліджували методом Х-променевої дифракції (XRD), а результати показали утворення чистої фази есколаїту Cr_2O_3 з ромбоедричною кристалічною структурою. Дослідження методом сканувальної електронної мікроскопії (SEM) показали, що при низьких енергіях лазера (300–400 мДж) процес сприяє утворенню менших та більш диспергованих частинок, оскільки енергії достатньо для абляції, але недостатньо для масштабного злиття частинок. Натомість вищі енергії лазера (500–600 мДж) призводять до формування більших частинок із підвищеною агрегацією, що, ймовірно, пов'язано з більшим тепловим внеском, посиленою дифузією та повторною нуклеацією наночастинок у рідкому середовищі. Оптичні дослідження показали незначне збільшення ширини забороненої зони зі зростанням потужності лазера, що пояснюється зсувом Бурштейна-Мосса, при якому рівень Фермі зміщується в зону провідності, змінюючи електронні переходи. Аналіз антибактеріальної активності підтвердив ефективність наночастинок щодо *Klebsiella pneumoniae*, *Escherichia coli* та *Staphylococcus epidermidis*. Водночас спостерігалася інша взаємодія між наночастинками оксиду хрому та клітинною структурою таких мікроорганізмів, як *Candida albicans* і *Staphylococcus aureus*, що проявлялося у зниженні їх антимікробної активності.

Ключові слова: антимікробна активність, PLA, наночастинки оксиду хрому, оптична ширина забороненої зони, структурна характеристика.